



# Experimental and Numerical Investigation of Hydrogen Embrittlement Effect on Microdamage Evolution of Advanced High-Strength Dual-Phase Steel

M. Asadipoor<sup>1,2</sup> · J. Kadkhodapour<sup>2</sup> · A. Pourkamali Anaraki<sup>2</sup> · S. M. H. Sharifi<sup>3</sup> · A. Ch. Darabi<sup>2,4</sup> · A. Barnoush<sup>1</sup>

Received: 10 January 2020 / Accepted: 3 March 2020 / Published online: 30 March 2020  
© The Korean Institute of Metals and Materials 2020, corrected publication 2020

## Abstract

The effect of hydrogen on the microdamage evolution of 1200M advanced high-strength steel was evaluated by the combination of experimental and numerical approaches. In the experimental section, the tensile test was performed under different testing conditions, i.e., vacuum, in-situ hydrogen plasma charging (IHPC), ex-situ electrochemical hydrogen charging (EEHC), and ex-situ + in-situ hydrogen charging (EIHC) conditions. The post-mortem analysis was conducted on the fracture surface of specimens to illuminate the impact of hydrogen on the microstructure and mechanical properties. The results showed that under all of hydrogen charging conditions, the yield stress and ultimate tensile strength were slightly sensitive to hydrogen, while tensile elongation was profoundly affected. While only ductile dimple features were observed on the fracture surfaces in vacuum condition, the results indicated a simultaneous action of the hydrogen-enhanced decohesion (HEDE) and hydrogen enhanced localized plasticity (HELP) mechanisms of HE, depending on the local concentration of hydrogen under the IHPC and EEHC conditions. At the EIHC condition, the HEDE model was the dominant failure mechanism, which was manifested by the HE-induced large crack. In the numerical approach, a finite-element analysis was developed to include the Gorson–Tvergaard–Needleman (GTN) damage model in Abaqus<sup>TM</sup> software. To numerically describe the damage mechanism, the GTN damage model was utilized in the 3D finite-element model. After calibration of damage parameters, the predicted damage mechanisms for two testing conditions, i.e., vacuum and EIHC, were compared with experimental results.

**Keywords** Hydrogen embrittlement · Ex-situ electrochemical hydrogen charging · In-situ hydrogen plasma charging · Damage evolution · GTN damage model

✉ A. Pourkamali Anaraki  
ali\_pourkamali@sru.ac.ir

M. Asadipoor  
Asadipoor.mohsen@gmail.com

J. Kadkhodapour  
javad.kad@gmail.com

S. M. H. Sharifi  
sharifi@put.ac.ir

A. Ch. Darabi  
ch.darabi@gmail.com

A. Barnoush  
afrooz.barnoush@ntnu.no

<sup>1</sup> Department of Mechanical and Industrial Engineering, Norwegian University of Science and Technology, 7491 Trondheim, Norway

<sup>2</sup> Department of Mechanical Engineering, Shahid Rajaei Teacher Training University, Tehran 16788-15811, Iran

<sup>3</sup> Department of Mechanical Engineering, Petroleum University of Technology, Abadan 63187-14317, Iran

<sup>4</sup> Materials Science and Strength of Materials, Institute for Materials Testing, University of Stuttgart, 70569 Stuttgart, Germany

## 1 Introduction

Advanced high-strength steels (AHSSs) are a new generation of steel categories providing attractive materials for various applications by offering a combination of contrasting mechanical properties, particularly high strength and ductility. The automotive industry is one of the most essential areas of AHSS application, where these materials can meet the requirements of CO<sub>2</sub> emission regulations as well as essential criteria such as stiffness, shaping, crash performance, and enhanced safety by decreasing weight [1, 2]. Although AHSSs have been on the road for many years, more studies are ongoing to meet the increasing demand for the enhancement of safety, efficiency, durability, and quality along with cost reduction. The AHSSs includes dual-phase (DP), complex-phase (CP), ferritic-bainitic (FB), martensitic (MS), transformation-induced plasticity (TRIP), quenching and partitioning (Q&P), hot-formed (HF), twinning-induced plasticity (TWIP), and high-strength low-alloy (HSLA) steels [3]. The combination of ferrite and martensite phases constitutes the microstructure of DP steels. The soft ferrite phase constructs the substrate of the microstructure with appropriate ductility. Moreover, the hard martensitic phase is distributed in the ferrite matrix and increases the strength and strain hardening. Therefore, the automotive parts made of high-strength dual-phase (HSDP) steels have a high capacity for energy absorption. The strength of HSDP steels depends on the volume fraction of the martensite phase in the microstructure. The increment of martensite volume relative to the ferrite matrix during the manufacturing process causes residual stress at the interfaces between ferrite and martensite. Accordingly, there is a high aggregation of mobile dislocations in the ferrite phase, contributing to improved efficiency [4].

Although AHSSs have individual and beneficial mechanical properties, their integrity may be threatened by hydrogen-induced reactions [5]. These materials lose ductility when exposed to hydrogen, resulting in hydrogen embrittlement (HE) phenomenon. Among the different types of AHSSs, the DP, TRIP, Q&P, and HSLA steels are extensively applied in the automotive construction, and therefore their interaction with hydrogen has been considerably investigated in the literature [3, 6–10]. For instance, Depover et al. [11], evaluated the effects of hydrogen on the mechanically induced degradation of AHSSs. They observed relatively low sensitivity to HE (about 8%) in HSLA steel containing useful compounds of Ti and Nb-based carbo-nitrides. The results also showed that the ductility of DP and TRIP steels decreased by about 54% and 60%, respectively, when exposed to hydrogen. Tensile tests were performed on these steels immediately after

hydrogen charging and after atmospherically discharging by Duprez et al. [12]. They found that the reduction of ductility was principally reversible for DP and TRIP steels because a considerable portion of the ductility was recovered after a week of discharging the tensile specimens, while the discrepancy between immediately charging and atmospherical discharging in HSLA steel was limited. These findings were related to the results of Escobar et al. [13], where thermal desorption spectroscopy (TDS) analysis was performed on these AHSSs. They applied various vacuum times before the beginning of TDS evaluation to investigate hydrogen emission. The results indicated that the hydrogen introduced in TRIP and DP steels was mostly dispersible and quickly left the material in a vacuum, whereas opposite effects were observed for HSLA steel. It was also demonstrated that the activation energy of various traps in the AHSSs was in a similar domain. These results represented a complicated relationship between a specific microstructural property and a particular desorption top point [14]. Furthermore, Laureys et al. [8, 9] conducted a comprehensive microstructural investigation on these AHSSs. Their results revealed that crack initiation occurred mostly in the interfaces of the martensitic matrix, and the cracking propagation factor was stress. Also, Davis [15] indicated that hydrogen affected fracture, starting in the hard martensite phase and extending to the soft ferrite matrix. It is worth mentioning that the considerable difference in the mechanical properties between the ferrite and martensite phases in DP steels leads to particular challenges in the existence of hydrogen [15]. Sun et al. [16] reported that the microstructural changes of DP steels during hydrogen charging initiate cracks along the interface and lath boundaries; therefore, they exhibited relatively high sensitivity to HE.

In the last decades, researchers have observed two typical damage mechanisms in micro-scale due to hydrogen charging: (1) the hydrogen plasticity mediated model and (2) the hydrogen-enhanced decohesion model (HEDE) [17, 18]. Several hydrogen plasticity mediated models were proposed by researchers, i.e., hydrogen-enhanced localized plasticity mechanism (HELP) [19], hydrogen-enhanced strain-induced vacancy (HESIV) [20, 21], adsorption-induced dislocation emission (AIDE) [22], and Defactant concept [23–25]. These mechanisms can be observed where the value of local hydrogen is very low and hydrogen helps to plasticity deformation mechanisms [18]. Martin et al. [26] have published a review of recent experimental and numerical studies on hydrogen enhance embrittlement based on HELP mechanisms. By increasing the local hydrogen concentration, the HEDE damage mechanism can be observed in the fracture surface and the high value of hydrogen concentration leads to brittle fracture behavior in metals [17, 27, 28]. In addition of HELP and HEDE mechanisms, two

multiple mechanisms were observed in steel materials: (a) HELP mediated HEDE mechanism, this damage model starts with HELP mechanisms and then finally it leads to HEDE mechanism [26, 29–31]; (b) HELP + HEDE, the both plasticity mediated and HEDE mechanisms can be observed in this failure model [17, 28, 32–39]. Djukic et al. [28] investigated the damage mechanisms in the failed boiler tubes due to high temperature hydrogen attack (HTHA). They reported that the damage mechanism was very dependent on local concentration of hydrogen in material. At region with low hydrogen concentration, micro void coalescence (MVC) mechanism observed in microstructure and HELP mechanism was more dominant. Whereas, as the hydrogen concentration increases, the HEDE mechanism was more effective. Consequently, at high local hydrogen concentration, HEDE mechanism was dominant and transgranular (TG), intergranular (IG) and micro-crack fracture modes occurred in the fracture surface. Djukic et al. [17] released a correlation between the value of local hydrogen concentration, macro-mechanical properties (i.e., impact strength and hardness) and damage mechanisms. They proposed a threshold value ( $CH_{(0)}$ ) and a critical value ( $CH_{(critical)}$ ) for local hydrogen concentration. Consequently, the local hydrogen concentration was divided into three zones. In zone 1, the value of local hydrogen concentration was lower than  $CH_{(0)}$ . In this region, the value of hydrogen was very low and the material was in safe condition and HELP mechanism was dominant. Whereas in zone 2, between  $CH_{(0)}$  and  $CH_{(critical)}$  values, the ductility decreases suddenly and the HEDE mechanism was more than HELP mechanism. At higher value of local hydrogen than  $CH_{(critical)}$  (zone 3), the HEDE mechanism was also dominant.

There has also been valuable research in the field of simulation and modeling. Song et al. [40] revealed the damage mechanism transition from ductile to brittle by molecular dynamics simulation. They illustrated that due to aggregation of hydrogen at the crack tip, the dislocation cannot be distributed and consequently, brittle-cleavage fracture happens in material by crack propagation. Falkenberg et al. [41] utilized a numerical model to predict the hydrogen-induced stress-corrosion cracking (HISCC) in a ferritic steel. The proposed model included the HELP and HEDE models. The obtained results had a good agreement with the experimental results. In another work, Jemblie et al. [42] simulated the hydrogen-induced cracking by cohesive zone model (CZM) and after CZM parameters calibration a good agreement was observed between the predicted numerical results and experimental results. However, they reported that this approach has some limitation that these results cannot be applied to other hydrogen system.

Kumar et al. [33] and Fan et al. [34] investigated the effect of hydrogen pre-charging and hydrogen charging during loading on mechanical behavior and damage

mechanisms of martensitic stainless steel. As the hydrogen pre-charging increases, the material ductility decreased and the yield stress remained unchanged and, also IG fracture mode increased on fracture surface. Whereas, as the hydrogen during loading increases, both yield stress and ductility decreased and fracture mode transferred from dimples to inter-granular. Consequently, for both hydrogen charging conditions, HEDE mechanism was dominant. Hu et al. [43] studied the damage mechanisms of hydrogen embrittlement in an ultra-high strength steel. The results illustrated that the damage mechanisms in the ultra-high strength steel after a slow strain rate test (SSRT) were micro void coalescence with few cracks inside the steel. At low value of the solution PH, the micro-crack initiation mechanism appeared on surface and also within the steel. Rehr et al. [36] studied the effect of hydrogen charging on mechanical behaviors of four different steels under two different loading rates. The results revealed that at low strain rate, due to hydrogen transport and hydrogen trapping by dislocation, HELP mediated HEDE model could be observed. Whereas, at high loading rate, due to the low value of hydrogen emission, hydrogen accumulation was insufficient and consequently, the ductile fracture behavior obtained for all grades of materials. Furthermore, Novak et al. [44] assessed the damage mechanism in a single edged notched four-point bending specimen. They illustrated the damage mechanism in martensitic steel HELP model due to MVC mode to completely HEDE model with IG fracture model as numerically and experimentally. In addition, Koyama et al. [32] evaluated the reaction of microcracks in ferrite-martensite DP steel in the attendance of hydrogen. Their findings indicated that hydrogen had a significant effect on the evolution of damage. The HELP and HEDE mechanisms were also applied to facilitate the evaluation of damage evolution in DP steels, resulting in an unpredictable HE failure.

Generally, a review of published papers demonstrated that the HEDE mechanism had been the preferred approach for continuum level HE simulation over the past decade. In this mechanism, the development of brittle fracture was associated with the reduction in the cohesive strength of the material lattice and was consistent with Griffith-type fracture [45]. Although the HEDE mechanism is still favored by models such as cohesive zone modeling (CZM) that appropriately exhibit the process of brittle fracture [46], the use of the HELP mechanism has become inevitable because of the complex microstructures and local mechanics of some materials such as DP steels. The studies revealed that the hydrogen-induced degradation of DP steels occurs after a considerable value of plastic strain, and the HELP mechanism claims that plasticity is enhanced locally by facilitating the activity of dislocation by hydrogen effect [47]. The continuum model based on the HELP mechanism has recently been developed. Yu et al. [48] found the criterion of

fracture related to hydrogen-affected shear band construction using representative material volume analysis. This criterion identified the failure in a small void volume fraction at low-stress triaxiality condition. It was observed that the HELP mechanism identifies hydrogen-induced premature failure with brittle fracture features. The results additionally showed that greater plasticity does not certainly lead to higher ductility. From the standpoint of micromechanical damage simulations, Gurson's model [49] is recognized as a popular tool for HE simulation based on the HELP continuum model. This damage model anticipates the failure behavior based on three steps, including void nucleation, void growth, and void coalescence. This model has been well developed and adapted over the past decades, resulting in alternative versions of failure prediction. A major version was produced by Tvergaard and Needleman [50] which was used in the present study. Recently, Yu et al. [45] developed this version by employing an additional hydrogen-related parameter into the Gurson model and presented a practical HE simulation tool according to the HELP model. In this mechanism, the interactions of hydrogen and microvoids were investigated by analyzing the unit cell with different concentrations of hydrogen. Also, the parameter calibration method of this model is straight and affordable for engineering applications.

A key strategy in studying the interactions of hydrogen and microstructure of materials is to evaluate the results of experiments and simulations in uncharged and charged specimens. Several experimental methods such as ex-situ electrochemical hydrogen charging (EEHC), gaseous hydrogen charging, and in-situ hydrogen plasma charging (IHPC) have been developed for hydrogen charging of specimens. The first and second methods are the traditional hydrogen charging methods, which have been investigated in many studies [51–63]. The third method is known as a modern hydrogen charging technique developed in recent years [64–66]. In the electrochemical hydrogen charging method, hydrogen release is achieved by immersing the sample in an acidic or alkaline solution as well as applying cathodic potential. Evaluation of hydrogen diffusion, hydrogen trapping, hydrogen concentration, and hydrogen-induced mechanical degradation are some of the applications of this method of hydrogen charging [3, 67, 68]. In the gaseous hydrogen charging method, the samples are subjected to the high pressure of hydrogen gas, and the variations of various parameters affected by hydrogen are investigated. Some examples of these studies can be found in Refs. [56–63]. In both traditional hydrogen charging methods, it is difficult to straightly observe the surface of the sample during deformation in the experiment. The IHPC method has been developed to overcome this problem [64, 65]. In this approach, the hydrogen fugacity increases with the conversion of hydrogen gas into hydrogen plasma, and accordingly, HE can be more accurately evaluated.

There is a fundamental challenge in evaluating the behavior of HE in materials, especially body-centered cubic (BCC) steels under the EEHC condition. The essential problem is that although the tests are performed as soon as possible after hydrogen charging, because of the high diffusion coefficient of hydrogen, a large amount of hydrogen is released from the crystal of the material [69]. Accordingly, the results may be associated with a percentage of error. However, finding an appropriate solution to overcome this challenge has been given little attention so far. The present study, therefore, attempted to solve this problem through a safe sample transfer method as well as a combined ex-situ and in-situ hydrogen charging method. In the following, the results of this combined hydrogen charging method will be compared with the results of other hydrogen charging methods.

Therefore, the object of this study was to evaluate the influence of hydrogen on the microdamage evolution of a particular advance high strength dual-phase steel. The evaluations were conducted on experimental and numerical approaches. In the experimental procedure, the hydrogen effect was investigated by applying the tensile tests under vacuum, IHPC, EEHC, and ex-situ + in-situ hydrogen charging (EIHC) conditions along with post-mortem analysis of fracture surface of specimens. Finally, in the numerical section, the GTN damage model was utilized in the 3D models in Abaqus software to predict the fracture behavior of DP steels under various testing conditions, and good agreement was observed between the experimental and numerical results.

## 2 Material and Experimental Procedure

### 2.1 Material Specification and Sample Preparation

The effect of H was investigated on the mechanical properties and surface fracture features of a specific AHSS, i.e., 1200M steel. The chemical composition of the principal elements in the as-received material was evaluated by using energy dispersive X-ray spectroscopy (EDS) as presented in Table 1. ThyssenKrupp Steel Europe AG provided the material in the form of a 7 mm thickness plate. Afterward, the tensile specimens with the tensile axis parallel to the sheet longitudinal (rolling) direction were machined by the electrical discharge machining (EDM). The geometry of dog bone-shaped samples is illustrated in Fig. 1.

The surface and edges of tensile specimens were ground and polished to eliminate any oxides and residual strains. This redaction is necessary because these oxides and strains

**Table 1** Chemical composition of the materials (wt%)

C	Si	Mn	P	S	Al
0.14	0.40	1.56	0.02	0.01	0.015



**Fig. 1** Tensile specimen geometry (mm)

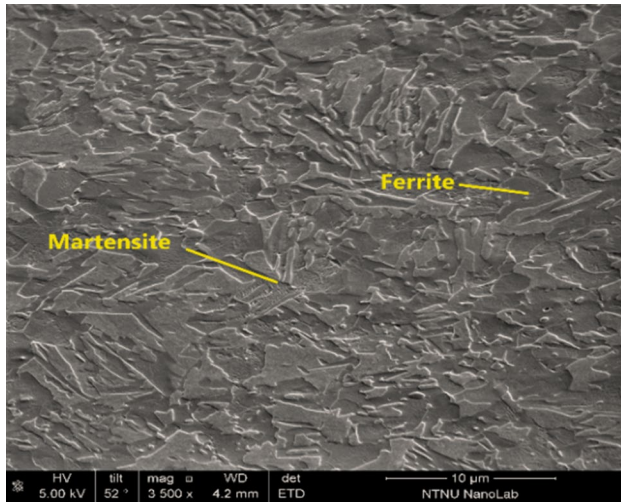
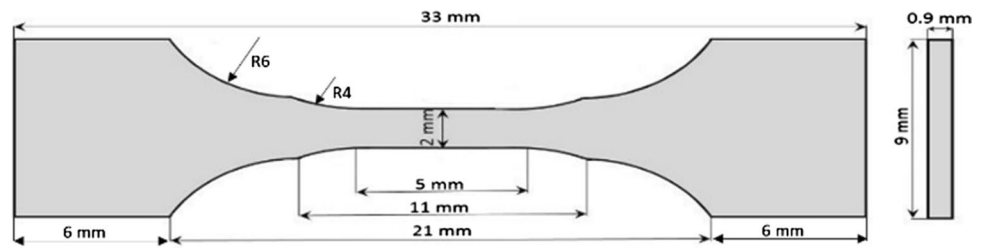


**Fig. 2** SEM image of 1200M DP steel

exert a preventing impact on the transport of hydrogen to the metal surface. The grinding process was performed up to #4000 abrasive paper and after that with 6  $\mu\text{m}$ , 3  $\mu\text{m}$ , and 1  $\mu\text{m}$  diamond paste polishing followed by final electropolishing.

## 2.2 Microstructure Characterization

The 1200M steel is an advanced HSDP steel with a combination of ferrite and martensite phases. The microstructure of 1200M steel consists of 60.8% ferrite and 39.2% martensite. The scanning electron microscope (SEM) micrograph of as-received 1200M DP steel is displayed in Fig. 2. It was observed that the corresponding grain sizes of ferritic and martensitic phases were about 7  $\mu\text{m}$  and 5  $\mu\text{m}$ , respectively.

## 2.3 Tensile Testing

Tensile experiments were conducted under vacuum, EEHC, IHPC, and the combination of ex-situ and in-situ conditions. A tensile modulus owned by Kamrath & Weiss GmbH was applied for tensile tests. This stage was embedded inside a Quanta 650 ESEM (Thermo Fisher Scientific Inc., USA). The engineering strain rate was selected

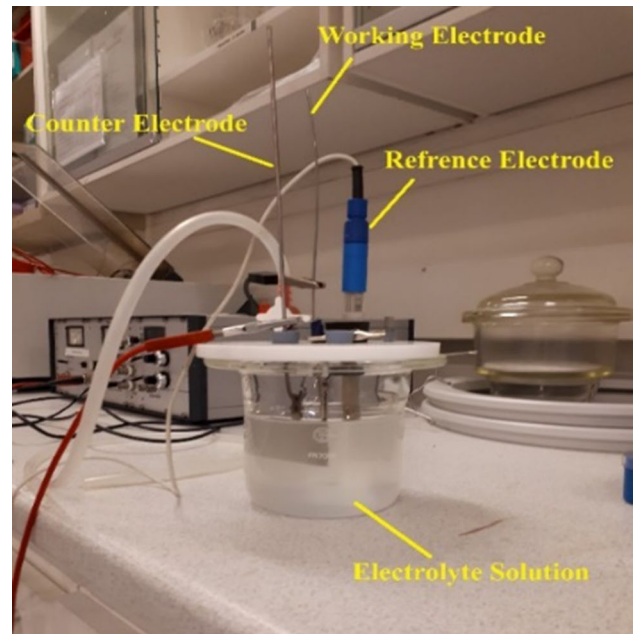


**Fig. 3** Setup of the EEHC test

to be  $10^{-5} \text{ s}^{-1}$  in order to provide uniformity in testing and sufficient time for diffusion and adsorption of hydrogen in hydrogen plasma charging tests.

### 2.3.1 Ex-Situ Electrochemical Hydrogen Charging Tensile Tests

The electrochemical cathodic hydrogen charging of the specimens was performed for 24 h and 48 h in a polycarbonate charging cell using a 0.05 M  $\text{Na}_2\text{SO}_4$  electrolyte solution. The charging process was performed using a conventional three-electrodes set up with the Ag/AgCl as the reference electrode, the tensile specimen as the working electrode, and a platinum grid as the counter electrode (Fig. 3). Hydrogen charging was performed in cathodic condition with the applied potential of  $-1500 \text{ mV}$  with respect to the reference electrode. This option does not create surface blisters or internal damage in the specimens, while the material is saturated with hydrogen.

### 2.3.2 In-Situ H-plasma Tensile Tests

In this step, an Evactron Model 25 Zephyr Plasma Cleaner (XEI Scientific, USA) with gaseous  $H_2$  as an output from a hydrogen generator was employed for H-charging. Also, a remote plasma was used in the cleaner to make only active plasma to participate in the interactions of the material. This setting was necessary to prevent the detrimental effects of the plasma afterglow on the material. The experimental setup of the in-situ H-plasma charging test is depicted in Fig. 4. Evidently, the plasma cleaner was connected to a hydrogen generator on one side and the SEM chamber on the other side. The tensile-compression module was installed into the SEM chamber, and it was connected to an exterior controlling system. Due to hydrogen flammability, imaging is unsafe under the low-pressure (high-voltage) environment of the SEM chamber. Accordingly, in this study, imaging could only be performed when the SEM chamber was vented to a high vacuum condition.

### 2.3.3 Ex-Situ + In-Situ Tensile Tests

In this step, a new test approach was combined with the two previous methods. First, the tensile specimen was charged by the EEHC method, and then it was transferred to the SEM chamber by putting the sample in a liquid nitrogen container. This protective method was adopted to prevent hydrogen release from the surface of the specimen. Finally,

the tensile test was performed under the in-situ H-plasma charging condition.

## 3 Numerical Method

Numerical analyses were conducted to investigate the effect of hydrogen charging on damage evolution parameters (e.g., porosity, nucleated void volume fraction, critical void volume fraction, and ductility). In this section, damage evolution is compared with experimental tensile test results under vacuum and EIHC conditions.

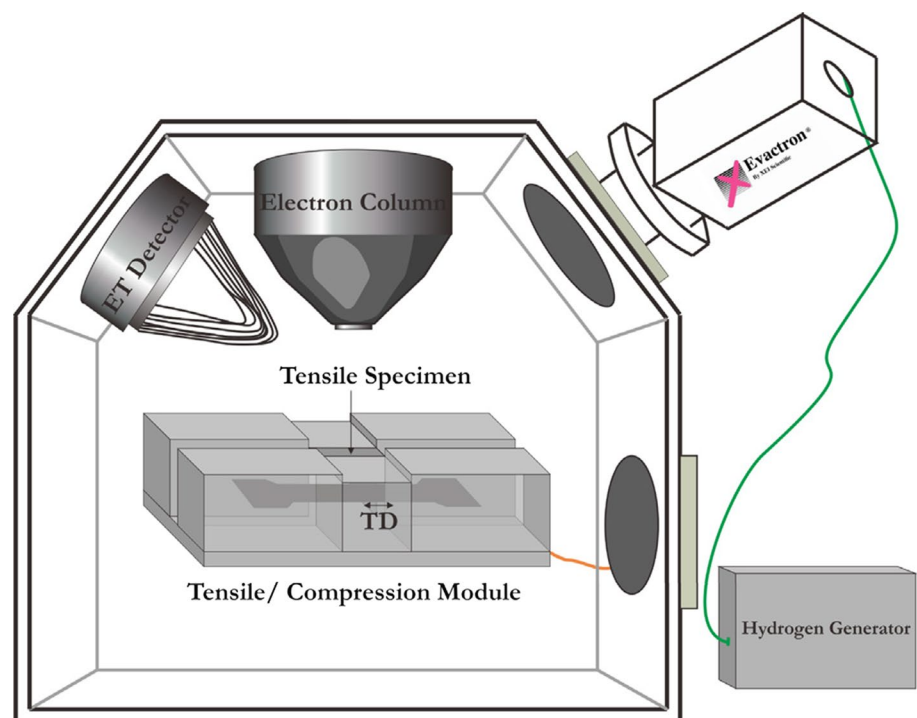
### 3.1 Finite-Element Analysis

In the first step, a three-dimensional (3D) simulation model, using the FE method in Abaqus software, was generated to analyze the tensile test behavior of 1200M steel. The isotropic behavior and J2 plasticity model were applied for material properties. Figure 5 depicts the meshed FE model using Abaqus software. The model consists of 27,504 C3D8 elements.

### 3.2 GTN Damage Modeling

From a micromechanical point of view, ductile fracture is the result of void initiation, void growth, void coalescence, and then final failure. To evaluate the effect of micromechanical parameters on ductile fracture under two testing

**Fig. 4** Experimental setup of in situ H-plasma charging test [64]



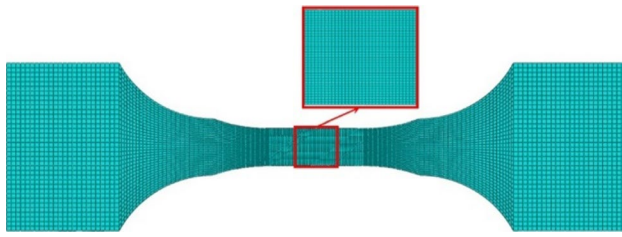


**Fig. 5** 3D FE model of the tensile test

conditions (vacuum and EIHC), the GTN damage model was applied for the FE model. The modified version of GTN damage suggested by Gurson [49] was adopted in this study. The GTN damage model is based on a yield potential function for a spherical void. In other words, this damage model examines the effect of void evolution on yielding behavior under different loading conditions. The GTN yield function is described as [50, 70]:

$$\phi = \left( \frac{\sigma_{eq}}{\sigma_y} \right) + 2q_1 f^* \cosh \left( \frac{3}{2} q_2 \frac{\sigma_m}{\sigma_y} \right) - (1 + q_3 f^{*2}) = 0 \quad (1)$$

where  $q_1$ ,  $q_2$ , and  $q_3$  are GTN damage fitting parameters proposed by Tvergaard [71];  $\sigma_m$  and  $\sigma_{eq}$  are hydrostatic stress and equivalent stress, respectively; and  $\sigma_y$  is material yield stress. Tvergaard and Needleman proposed function  $f^*$  to decrease the loss of load-carrying capacity due to void growth and coalescence.

$$f^* = \begin{cases} f & \text{for } f < f_c \\ f_c + \frac{1}{f_f - f_c} (f - f_c) & \text{for } f > f_c \end{cases} \quad (2)$$

Here,  $f$  is void volume fraction and  $f_c$  and  $f_f$  are critical void volume fractions at the beginning of void coalescence and failure, in that order [72]. In this damage model, the sum of the void growth volume fraction and the nucleated new voids are considered as the total void volume fraction evolution.

$$\dot{f} = (\dot{f})_g + (\dot{f})_n = (1 - f) \cdot \dot{\epsilon}_{kk} + \frac{f_N}{S_N \sqrt{2\pi}} \exp \left[ -\frac{1}{2} \left( \frac{\bar{\epsilon} - \epsilon_N}{S_N} \right)^2 \right] \bar{\epsilon} \quad (3)$$

where  $(\dot{f})_g$  and  $(\dot{f})_n$  are the volume fraction of the void growth and void nucleation, respectively;  $f_N$  and  $S_N$  are the volume fraction of secondary voids and the plastic strain deviation, in that order;  $\dot{\epsilon}_{kk}$  and  $\bar{\epsilon}$  are the rate of plastic strain and the rate of equivalent plastic strain, respectively; and  $\bar{\epsilon}$  and  $\epsilon_N$  are respectively the equivalent plastic strain and the mean value plastic strain. In this study, for material testing in vacuum conditions,  $q_1$ ,  $q_2$ , and  $q_3$  were considered equal to 1.3, 0.85, and 1.69, respectively, as proposed for

the ferritic-martensitic steel in Ref. [73]. Moreover,  $S_N$  and  $\epsilon_N$  were both assumed to be 0.2 [74]. Other parameters were calibrated based on Table 2. These ranges were extracted from several scientific reports [75–79].

Some researchers reported that hydrogen charging increases the void formation during loading condition. Morrissey et al. [80] investigated experimentally the effect of hydrogen charging on the initial void fraction by a computed tomography technique. They revealed that hydrogen charging significantly increases the initial void volume fraction, and this value increases up to near 0.01. Maire et al. [81] and Kumamoto et al. [82] showed that the void nucleation and void growth, are slightly affected by hydrogen charging. Consequently, the range of volume fraction of void nucleation and void growth were determined as same as without hydrogen charging condition. Koyama et al. [58] and Kumamoto et al. [82] illustrated that the local plastic strain decreases strongly by hydrogen charging in different damage evolution stages. Hence, a range value was considered for the  $\epsilon_N$  parameter based on Refs. [58, 82]. for 1200M steel under hydrogen charging. Table 3 presents the ranges of GTN damage parameters for 1200M steel under hydrogen charging.

### 3.3 Damage Calibration by Design of Experiment (DOE) Method

To use the GTN damage model, several parameters need to be calibrated and, therefore, traditional methods are not suitable for damage calibration. Several researchers have utilized the neural network method for GTN damage calibration [83,

**Table 2** GTN damage parameters for 1200M steel without hydrogen charging

GTN parameters	Minimum value	Maximum value
$f_0$	0.0003	0.0076
$\epsilon_N$	0.2	
$f_N$	0.008	0.015
$f_c$	0.015	0.025
$f_f$	0.025	0.04

**Table 3** GTN damage parameters for 1200M steel under hydrogen charging

GTN parameters	Minimum value	Maximum value
$f_0$	0.004	0.01
$\epsilon_N$	0.02	0.1
$f_N$	0.01	0.015
$f_c$	0.015	0.025
$f_f$	0.025	0.04

84]. In this paper, a central composite design (CCD) was applied to study the effect of GTN damage model parameters on fracture strain. The parametric study was conducted on four parameters at five levels for vacuum testing conditions, and five parameters at five levels for the ex-situ + in-situ conditions. Thirty and 48 tensile tests were simulated for vacuum and ex-situ + in-situ conditions, respectively, by the principle of response surface methodology (RSM) using Design-Expert software. This technique typically helps find the optimum damage parameters. Figure 6 demonstrates the damage calibration procedure with the RSM. In this method, damage parameters were optimized based on the difference in fracture strain values between the experimental and the simulation results.

## 4 Results and Discussion

### 4.1 Results of Tensile Tests

The tensile test results of 1200M steel under vacuum, in-situ H-plasma charging, EEHC, and the combination of ex-situ and in-situ hydrogen charging conditions are shown in Fig. 7. The H-plasma charging test was performed by starting the tensile test and then stopping at 50% of the ultimate tensile strength (UTS) range for 1 h and the UTS for 3 h. It must be noted that this stopping process was performed to provide further time for hydrogen diffusion into the crystal under increased solubility influence of the tensile stress. In addition to the in-situ H-plasma charging method as a novel

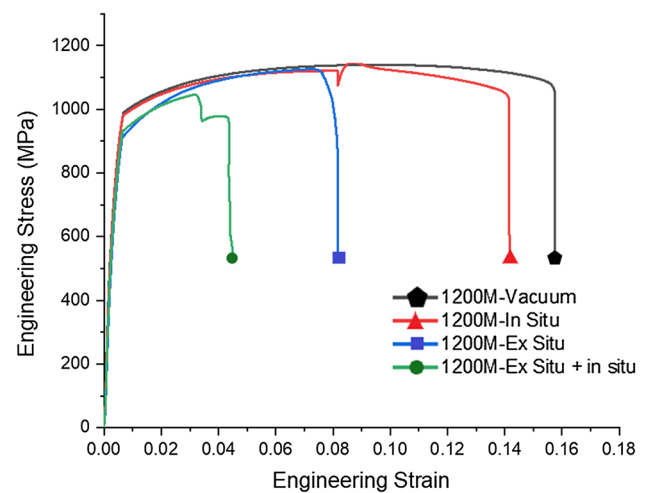


Fig. 7 Stress–strain results of the tested specimens under vacuum, in-situ, ex-situ, and ex-in situ conditions

hydrogen charging technique, the EEHC as a traditional hydrogen charging method along with a combination of in-situ and ex-situ hydrogen charging methods were employed to evaluate the HE susceptibility of 1200M steel.

The flow stress curve of the vacuum test revealed that the yield stress (Y.S) and UTS of 1200M steel were about 990 MPa and 1140 MPa, respectively. These results are in good agreement with the material standard specification [85]. The standard corroborates that the steels with Y.S below 400 MPa are protected against HE. Accordingly, as shown in Fig. 7, the behavior of tested samples under

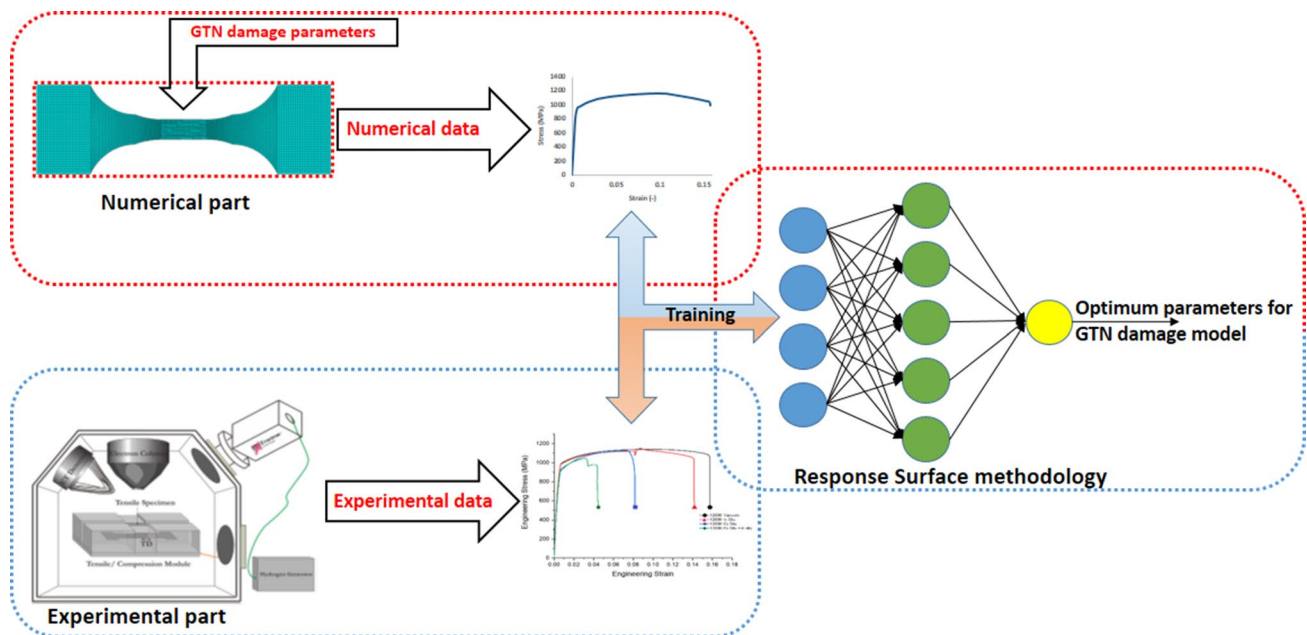


Fig. 6 Damage parameters calibration procedure using the DOE methodology



H-charging conditions was similar to the vacuum condition in the elastic region until about 400 MPa, after which the deviations of the stress flow curves commenced and continued in the plastic area. The quantitative results of the tensile tests, including Y.S, UTS, and elongation to failure, before and after H-charging are given in Table 4. It is observed that the Y.S and UTS were slightly sensitive to HE while tensile elongation was highly affected. Accordingly, the results showed that the tensile samples under in-situ, ex-situ, and combined ex situ-in situ hydrogen charging conditions had a reduction in the yield strength of about 1%, 8%, and 7%, respectively, compared to the vacuum condition. Moreover, they had a reduction in the ultimate tensile strength of about 0%, 1%, and 8% compared to the vacuum condition. The introduction of hydrogen in the in-situ, ex-situ, and combined ex situ-in situ tests caused reductions in tensile elongation by about 10%, 48%, and 69.6%, respectively, in comparison with the reference vacuum test.

## 4.2 Fractographic Analysis

The microcosmic morphology of the tensile fracture surfaces of 1200M steel under vacuum, IHPC, EEHC, and combination of IHPC and EEHC conditions is displayed in Fig. 8.

The analysis of the fracture surfaces of tensile specimens in the vacuum condition represented that the HELP model was the dominant failure mechanism in samples. Figures 8b, c show the magnified ductile features of 1200M specimens in vacuum conditions. The micro-voids (MV) and uniform ductile dimples (DD) pattern can be found as a significant area fraction of fracture surface in specimens. These features suggest that the process of crack initiation and propagation was in a more ductile manner when hydrogen was not present.

The enlarged fracture surfaces of the tensile specimens after final fracture under the in-situ hydrogen plasma charging (IHPC) conditions are exhibited in Fig. 8e, f. These high-resolution images show the morphology of quasi-cleavage (QC) facets and micro-cracks in the fractured surfaces after H-charging in addition to micro-voids coalescence (MVC) and dimples. As shown in Fig. 8e, a mix of two types of crack propagation, including intergranular

(IG) and transgranular (TG) cracking, can be distinguished on fracture surfaces. The TG cracks are created by increasing the concentrations of hydrogen in local areas, where the emission and motion of dislocations would be increased and the cohesion of Fe–Fe bonds could be decreased. In some regions, the hydrogen trapped at grain boundaries (GB) and it has an essential role in the hydrogen degradation processes of steels and caused IG fracture by reducing the strength of GB according to the HEDE + HEDE mechanism [17, 18, 28]. In fact, when the concentrations of hydrogen are low, the accumulation of hydrogen in the GBs is also possible and the cracks initiate more at the grain boundaries, resulting in IG cracking [86].

These TG and IG micro-cracks and QC features principally illustrate the occurrence of brittle fracture in local areas. However, the ductile fracture modes i.e. MVC and dimples are in a larger part of fracture surface and brittle fracture modes i.e., QC and micro-cracks are in smaller region [17, 28]. These findings demonstrated that the material ductility has decreased slightly compared to vacuum condition and both damage mechanisms (HELP and HEDE) could be observed in the fracture surface and due to low value of local hydrogen concentration, the HELP mechanism is more common than HEDE (HELP > HEDE).

Figure 8h, i characterize the magnified fracture surfaces of the tensile specimens of 1200M steel after final fracture under the EEHC condition. In these ESEM images, the brittle fracture features, including QC, IG and TG micro-cracks and river-like cleavage (RC) patterns, along with ductile fracture mode (MVC) are observed. A comparison of these features indicated that the brittle fracture mode is dominant compare to ductile fracture features (IG + TG + RC >> MVC). This is a result of the increased activity of the HEDE mechanism compared to HELP mechanism (HEDE > HELP), according to the proposed HELP + HEDE model [17, 18, 28].

Finally, the fracture surface appearance of a tensile specimen after the final fracture under the EIHC condition is exhibited in Fig. 8j. It is observed that a large crack is created at the center-line of the fracture surface. In this testing condition, the value of local hydrogen concentration increases and the lowest ductility were observed. Here, increasing the number of IG and TG fracture modes joining them together as well as the coalescence of the micro-cracks and cleavage mechanism can be considered as the HEDE dominance damage mechanism.

## 4.3 Numerical Results

The comparison of the fracture morphologies of 1200M specimens in Fig. 8 revealed that the damages including micro-voids and micro-cracks developed from vacuum to hydrogen charged conditions, where the damage evolution

**Table 4** Tensile test results of 1200M steel under vacuum, in-situ, ex-situ and ex-in situ conditions

1200M steel	Yield strength (YS) (MPa)	Ultimate tensile strength (UTS) (MPa)	Elongation to failure (EF) (%)
Vacuum	990 ± 10	1140 ± 15	15.8 ± 1.5
In situ	980 ± 5	1140 ± 10	14.2 ± 1.2
Ex situ	910 ± 5	1130 ± 10	8.2 ± 0.8
Ex situ + in situ	920 ± 8	1050 ± 12	4.8 ± 1.1

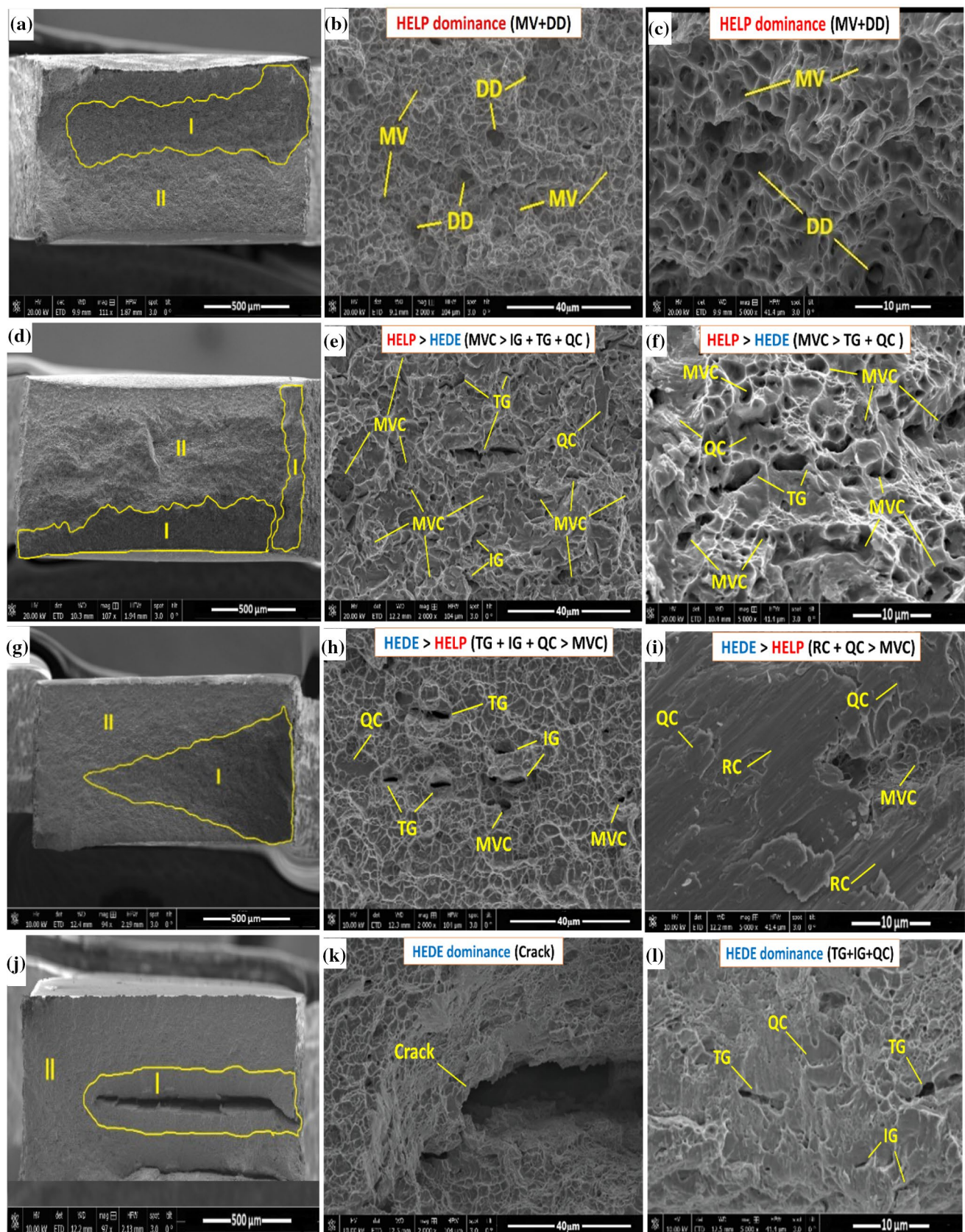


**Fig. 8** Fracture morphologies of 1200M steel specimens under **a** vacuum, **d** in-situ, **g** ex-situ, and **j** ex-situ + in-situ conditions, **b, c, e, f, h, i, k, l** enlarged images of the (I, II) marked area in images (**a, d, g, j**), respectively



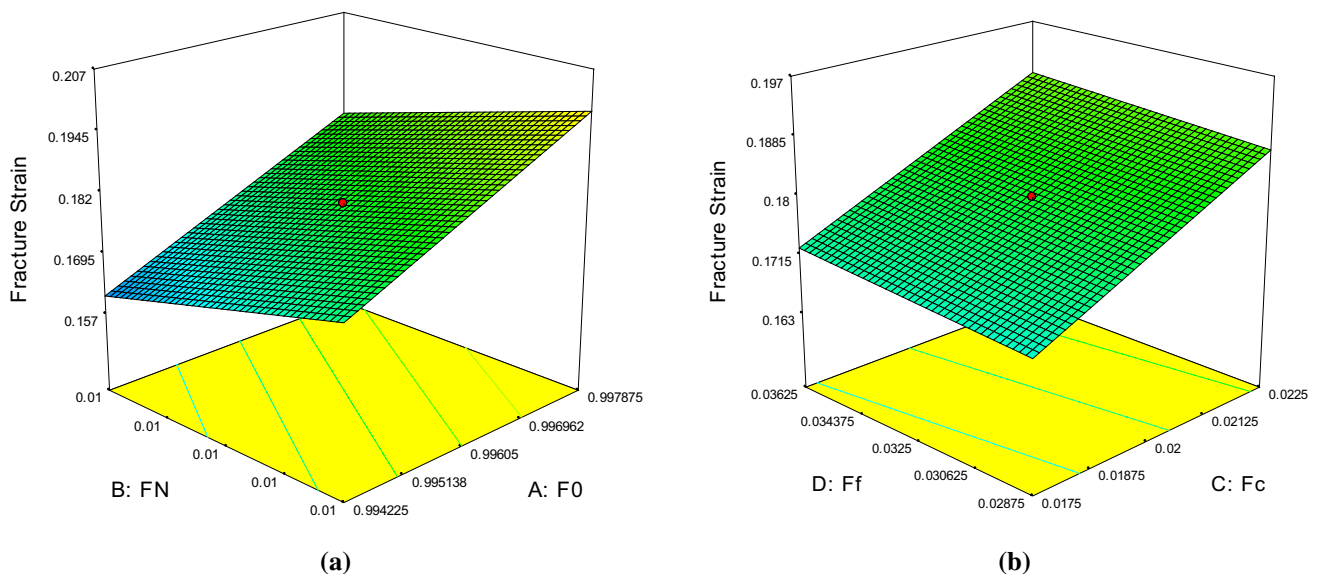
eventually resulted in the formation of HIC. Therefore, the effect of hydrogen on damage evolution was simulated using the GTN damage model and compared with the experimental results. Figures 9 and 10 illustrate the effect of damage parameters on fracture strain ( $\epsilon_f$ ) for vacuum and ex-situ + in-situ conditions, respectively. The linear regression model based on the experimental results is illustrated in Eqs. 4 and 5, and the precision of these equations in fitting the data equals 90% and 93%, respectively. The results showed that, as  $f_c$  and  $f_f$  increased, the fracture strain increased, and decreasing parameters  $f_0$ ,  $f_n$ , and  $\epsilon_n$  increased the fracture strain in both testing conditions. The initial void volume fraction ( $f_0$ ) was the most effective parameter on fracture strain, followed by  $f_n$  and  $f_c$  which had a stronger influence on fracture behavior for

both testing conditions. Furthermore, fracture strain had a weak dependence on  $f_f$  and  $\epsilon_n$ .

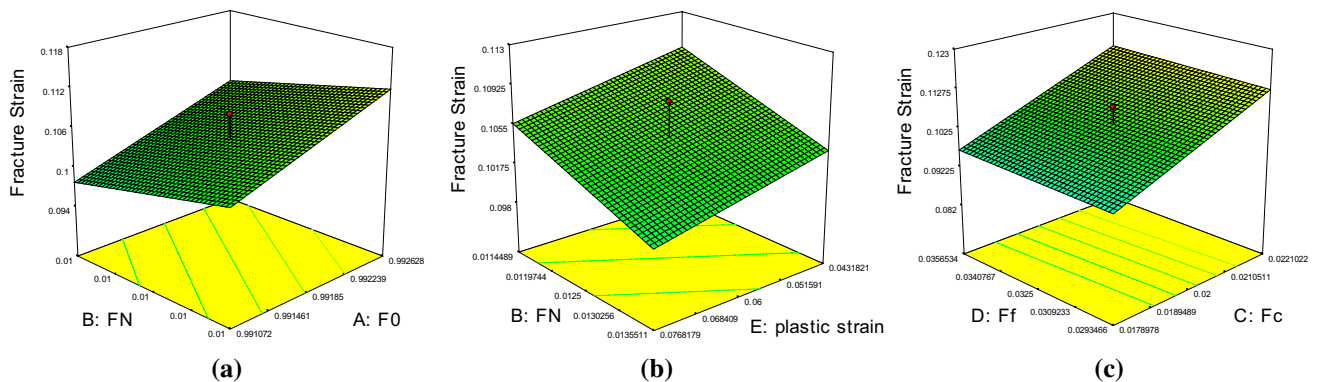
$$\epsilon_f = -6.36500 + 6.54062 \times (1 - f_0) - 3.99712 \times f_n + 3.28798 \times f_c + 0.31199 \times f_f \quad (4)$$

$$\epsilon_f = -5.49699 + 5.60111 \times (1 - f_0) - 2.57384 \times f_n + 4.00398 \times f_c + 0.15740 \times f_f - 0.11078 \times \epsilon_n \quad (5)$$

Table 5 presents the optimum damage parameters of the GTN model, obtained by RSM. It can be observed from Fig. 11 that the 3D numerical model with optimum damage parameters has more acceptable results with an



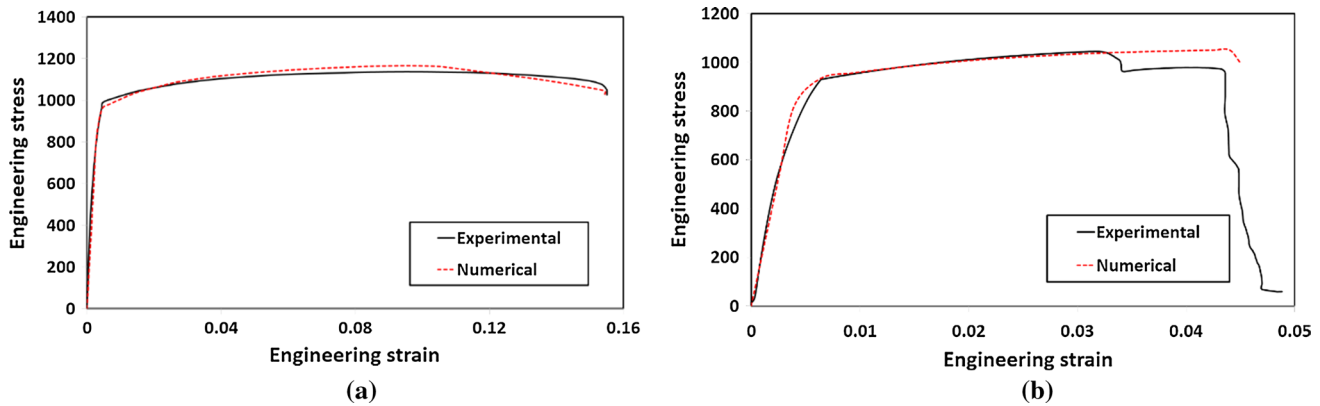
**Fig. 9** The effect of **a**  $f_0$ ,  $f_n$  and **b**  $f_c$ ,  $f_f$  on the fracture strain predicted by the GTN damage model for the tensile specimen under vacuum testing condition



**Fig. 10** The effect of **a**  $f_0$ ,  $f_n$  and  $f_n$ , **b** plastic strain at the beginning of void nucleation, and **c**  $f_c$ ,  $f_f$  on the fracture strain predicted by the GTN damage model for the tensile specimen under ex-situ + in-situ testing condition

**Table 5** Optimum parameters of the GTN model

	$q_1$	$q_2$	$q_3$	$f_0$	$f_n$	$\epsilon_n$	$S_N$	$f_c$	$f_f$
Vacuum	1.3	0.85	1.69	0.0076	0.0115	0.2	0.2	0.02	0.0325
Ex-situ + in-situ	1.3	0.85	1.69	0.01	0.015	0.0768	0.2	0.015	0.025

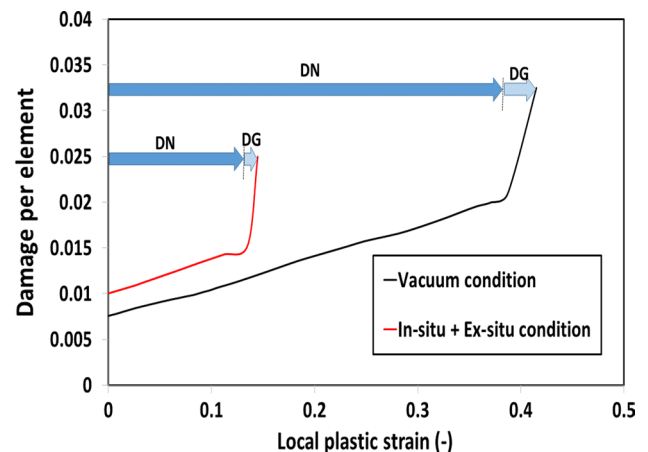
**Fig. 11** Comparing the results obtained from the numerical model in conjunction with the GTN damage model with an experimental stress–strain curve under **a** vacuum testing condition and **b** hydrogen charging condition

error of 3.06 and 1.2% for vacuum and ex-situ + in-situ conditions, respectively.

According to Table 5, the ductile damage evolution parameters (i.e., initial void fraction, nucleation void fraction, critical void fraction, and local plastic strain) could be compared to each other. Based on the results, with hydrogen charging, the initial damage fraction and nucleated damage fraction increased roughly by 31.6% and 30.4%, respectively. The numerical results reveal that increasing the value of initial void fraction has important influence in earlier fracture in metal that already revealed by Morrissey et al. [80] and Maire et al. [81] experimentally. They reported that the hydrogen charging increases the initial void size and void fraction and these parameters are very depending on hydrogen concentration.

The critical void volume fraction at coalescence, critical void volume fraction at fracture, and local plastic strain at the beginning of void nucleation decreased by about 25%, 23.7%, and 61.6%, respectively. As reported in Refs. [87, 88], due to the existence of brittle fracture modes in hydrogen charged specimens, the voids easier to coalesce. Consequently, the value of  $f_c$  and  $f_f$  decreased for hydrogen charging condition. The results indicated that the local plastic strain at the beginning of damage nucleation under the ex-situ + in-situ condition was significantly reduced which the same results were observed by Maire et al. [81] and Koyama et al. [58] as experimentally.

Figure 12 demonstrates the damage evolution to local plastic strain. The damage evolution can be divided to two stages: (i) damage nucleation (DN), and (ii) damage

**Fig. 12** Damage evolution to local plastic strain curves under vacuum and in-situ + ex-situ hydrogen charging condition

propagation (DG). In this study, the initial void fraction considered as initial damage fraction as same as Maire et al. [81], whereas Koyama et al. [58] neglected initial void. Figure 12 illustrates that the nucleated void volume fraction under the ex-situ + in-situ condition is less than vacuum condition. Further damage propagation rate in ex-situ + in-situ condition is more than vacuum condition, which reveals a brittle behavior at damage propagation stage for ex-situ + in-situ condition.

Figure 13 shows the equivalent plastic strain distribution at the fracture point for both testing conditions, and the results were compared with experimental results. Evidently,



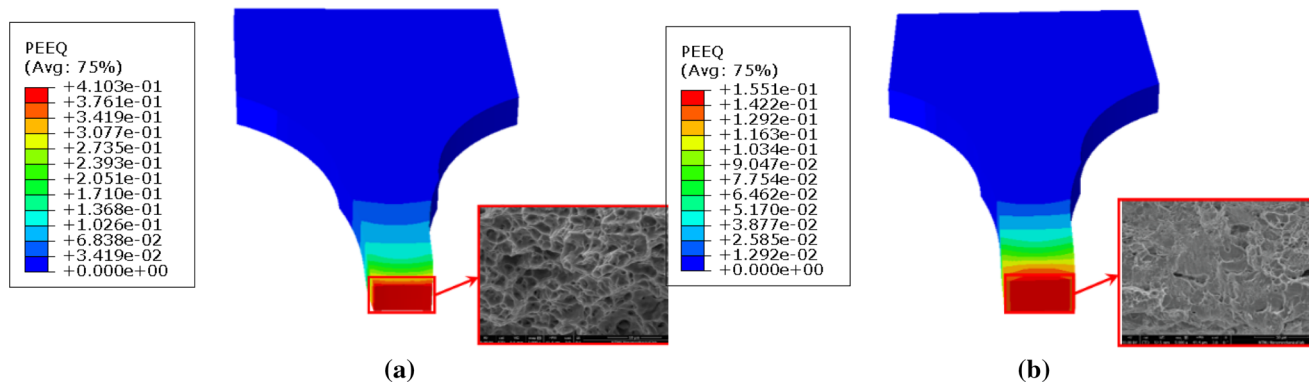


**Fig. 13** Equivalent plastic strain distribution at the fracture point, for **a** vacuum testing condition, and **b** ex-situ + in-situ testing condition

without hydrogen charging, the damage behavior is completely ductile and HELP dominance. Here, the failure features are void growth and void coalescence mechanisms.

The numerical results in Fig. 13b show that with hydrogen charging, the ductility sharply reduces and consequently the damage mechanism transits from HELP to the HEDE dominance. In other words, under in-situ + ex-situ testing condition, the material has HEDE + HEDE damage behavior, which HEDE mechanism is very more dominant. Hence, the number of IG and TG fracture modes increase in material. Consequently, MVC fracture mode does not have enough time to grow; before that, IG and TG fracture modes joint together as well as the coalescence of the micro-cracks and cleavage mechanism lead to HEDE dominance damage model.

## 5 Conclusion

In the present study, a combination of experimental and numerical approaches was employed to evaluate the effect of hydrogen on microdamage evolution in 1200M advanced high-strength steel. Several tensile tests under vacuum, IHPC, EEHC, and EIHC conditions were performed on the specimens. Moreover, the GTN damage model was applied to evaluate the effect of hydrogen charging on damage evolution and final failure. According to the results, the following conclusions can be drawn:

1. The variations of Y.S and UTS in the stress–strain curves were slight in all conditions, while the differences in the tensile elongation were profoundly affected.
2. At the vacuum condition, the HELP model was the dominant failure mechanism, which was manifested by ductile features such as micro-voids (MV) and uniform ductile dimples (DD).
3. A coexistence of the HE mechanisms (HELP + HEDE) was identified under the IHPC and EEHC conditions. At

the IHPC condition, the HELP mechanism was dominant compare to HEDE mechanism (HELP > HEDE), which was manifested by an increase in ductile MVC fracture features in the QC fracture surface (MVC > IG + TG + QC). While at the EEHC condition, the brittle fracture modes were dominant compare to ductile fracture features (IG + TG + RC > MVC) and the HEDE mechanism was more common than HELP mechanism (HEDE > HELP).

4. At the EIHC condition, the HEDE model was the dominant failure mechanism, which was manifested by increasing the value of local hydrogen concentration and the number of IG and TG fracture modes as well as the HE-induced large crack.
5. The damage scenario was numerically assessed under vacuum and in-situ + ex-situ testing conditions in three stages (i.e., initial damage, damage growth, and damage coalescence). After calibration, the results showed that hydrogen charging has an important effect on the initial void before applying loading and damage nucleation. The results show that the damage evolution can be divided to two stages: (i) damage nucleation (DN), and (ii) damage propagation (DG). The both stages will be longer for vacuum testing condition, due to more ductile behavior. For vacuum testing condition the material has a MVC fracture mode and HEDE damage model only could be observed at fracture surface. Whereas, with hydrogen charging (in-situ + ex-situ condition) the ductility strongly decreases and damage model transits from HELP to the HEDE dominance. Here, the existence of IG, TG and micro-crack fracture modes are the most reasons for brittle behavior.

**Acknowledgements** The Research Council of Norway is acknowledged for the support through the HyF-Lex (244068/E30) project.

**Data availability** The raw/processed data required to reproduce these findings cannot be shared at this time as the data also forms part of an ongoing study.

## Compliance with Ethical Standards

**Conflict of interest** The authors declare that there is no conflict of interest regarding the publication of this paper.

## References

1. D. Bhattacharya, Developments in advanced high strength steels, in *Proceedings of Proceedings of the Joint International Conference of HSLA Steels*, Sanya (2005), pp. 70–73
2. BC De Cooman, L. Chen, HS Kim, Y. Estrin, SK Kim, H. Voswinckel, State-of-the-science of high manganese TWIP steels for automotive applications, in *Microstructure and Texture in Steels* (2009), pp. 165–183
3. Q. Liu, J. Venezuela, M. Zhang, Q. Zhou, A. Atrens, Hydrogen trapping in some advanced high strength steels. *Corros. Sci.* **111**, 770–785 (2016)
4. T. Depover, F. Verduyck, A. Elmahdy, P. Verleysen, K. Verbeken, Evaluation of the hydrogen embrittlement susceptibility in DP steel under static and dynamic tensile conditions. *Int. J. Impact Eng.* **123**, 118–125 (2019)
5. M. Loidl, O. Kolk, Hydrogen Embrittlement in HSSs Limits Use in Lightweight Body in White Design-High strength steels (HSSs) can fail due to hydrogen embrittlement under certain circumstances, which hinders their use in the body in white design. *Adv. Mater. Process.* **169**(3), 22 (2011)
6. J.H. Ryu, Y.S. Chun, C.S. Lee, H.K.D.H. Bhadeshia, D.W. Suh, Effect of deformation on hydrogen trapping and effusion in TRIP-assisted steel. *Acta Mater.* **60**(10), 4085–4092 (2012)
7. J. Sun, T. Jiang, Y. Sun, Y. Wang, Y. Liu, A lamellar structured ultrafine grain ferrite-martensite dual-phase steel and its resistance to hydrogen embrittlement. *J. Alloys Compd.* **698**, 390–399 (2017)
8. A. Laureys, T. Depover, R. Petrov, K. Verbeken, Characterization of hydrogen-induced cracking in TRIP-assisted steels. *Int. J. Hydrogen Energy* **40**(47), 16901–16912 (2015)
9. A. Laureys, T. Depover, R. Petrov, K. Verbeken, Microstructural characterization of hydrogen-induced cracking in TRIP-assisted steel by EBSD. *Mater. Charact.* **112**, 169–179 (2016)
10. J.A. Ronevich, J.G. Speer, D.K. Matlock, Hydrogen embrittlement of commercially produced advanced high strength sheet steels. *SAE Int. J. Mater. Manuf.* **3**(1), 255–267 (2010)
11. T. Depover, D.P. Escobar, E. Wallaert, Z. Zermout, K. Verbeken, Effect of hydrogen charging on the mechanical properties of advanced high strength steels. *Int. J. Hydrogen Energy* **39**(9), 4647–4656 (2014)
12. L. Duprez, K. Verbeken, M. Verhaege, Effect of hydrogen on the mechanical properties of multiphase high strength steels, in *Effect of Hydrogen on Materials* (2009), pp. 62–69
13. D.P. Escobar, K. Verbeken, L. Duprez, M. Verhaege, Evaluation of hydrogen trapping in high strength steels by thermal desorption spectroscopy. *Mater. Sci. Eng. A* **551**, 50–58 (2012)
14. D.P. Escobar, T. Depover, L. Duprez, K. Verbeken, M. Verhaege, Combined thermal desorption spectroscopy, differential scanning calorimetry, scanning electron microscopy, and X-ray diffraction study of hydrogen trapping in cold deformed TRIP steel. *Acta Mater.* **60**(6–7), 2593–2605 (2012)
15. R.G. Davies, Hydrogen embrittlement of dual-phase steels. *Metall. Trans. A* **12**(9), 1667–1672 (1981)
16. S. Sun, J. Gu, N. Chen, The influence of hydrogen on the substructure of the martensite and ferrite dual-phase steel. *Scr. Metall.* **23**(10), 1735–1737 (1989)
17. M.B. Djukic, G.M. Bakic, V.S. Zeravcic, A. Sedmak, B. Rajicic, Hydrogen embrittlement of industrial components: prediction, prevention, and models. *Corrosion* **72**(7), 943–961 (2016)
18. M.B. Djukic, G.M. Bakic, V.S. Zeravcic, A. Sedmak, B. Rajicic, The synergistic action and interplay of hydrogen embrittlement mechanisms in steels and iron: localized plasticity and decohesion. *Eng. Fract. Mech.* **216**, 106528 (2019)
19. R.P. Gangloff, B.P. Somerday (eds.), *Gaseous hydrogen embrittlement of materials in energy technologies: the problem, its characterization and effects on particular alloy classes* (Elsevier, Amsterdam, 2012)
20. M. Nagumo, *Fundamentals of hydrogen embrittlement* (Springer, Singapore, 2016), p. 239
21. M. Nagumo, Hydrogen related failure of steels—a new aspect. *Mater. Sci. Technol.* **20**(8), 940–950 (2004)
22. S.P. Lynch, Hydrogen embrittlement (HE) phenomena and mechanisms, *Stress corrosion cracking* (Woodhead Publishing, Sawston, 2011), pp. 90–130
23. A. Barnoush, H. Vehoff, Recent developments in the study of hydrogen embrittlement: hydrogen effect on dislocation nucleation. *Acta Mater.* **58**(16), 5274–5285 (2010)
24. A. Barnoush, H. Vehoff, In situ electrochemical nanoindentation: A technique for local examination of hydrogen embrittlement. *Corros. Sci.* **50**(1), 259–267 (2008)
25. R. Kirchheim, Revisiting hydrogen embrittlement models and hydrogen-induced homogeneous nucleation of dislocations. *Scr. Mater.* **62**(2), 67–70 (2010)
26. M.L. Martin, M. Dadfarnia, A. Nagao, S. Wang, P. Sofronis, Enumeration of the hydrogen-enhanced localized plasticity mechanism for hydrogen embrittlement in structural materials. *Acta Mater.* **165**, 734–750 (2019)
27. BN Popov, JW Lee, MB Djukic, Hydrogen permeation and hydrogen-induced cracking, in *Handbook of Environmental Degradation of Materials* (William Andrew Publishing, 2018), pp. 133–162.
28. M.B. Djukic, V.S. Zeravcic, G.M. Bakic, A. Sedmak, B. Rajicic, Hydrogen damage of steels: a case study and hydrogen embrittlement model. *Eng. Fail. Anal.* **58**, 485–498 (2015)
29. M.L. Martin, I.M. Robertson, P. Sofronis, Interpreting hydrogen-induced fracture surfaces in terms of deformation processes: a new approach. *Acta Mater.* **59**(9), 3680–3687 (2011)
30. A. Nagao, M. Dadfarnia, B.P. Somerday, P. Sofronis, R.O. Ritchie, Hydrogen-enhanced-plasticity mediated decohesion for hydrogen-induced intergranular and “quasi-cleavage” fracture of lath martensitic steels. *J. Mech. Phys. Solids* **112**, 403–430 (2018)
31. I.M. Dmytrakh, A.M. Syrotyuk, R.L. Leshchak, Specific features of the deformation and fracture of low-alloy steels in hydrogen-containing media: influence of hydrogen concentration in the metal. *Mater. Sci.* **54**(3), 295–308 (2018)
32. M. Koyama, C.C. Tasan, E. Akiyama, K. Tszaki, D. Raabe, Hydrogen-assisted decohesion and localized plasticity in dual-phase steel. *Acta Mater.* **70**, 174–187 (2014)
33. B.S. Kumar, V. Kain, M. Singh, B. Vishwanadh, Influence of hydrogen on mechanical properties and fracture of tempered 13 wt% Cr martensitic stainless steel. *Mater. Sci. Eng. A* **700**, 140–151 (2017)
34. Y.H. Fan, B. Zhang, H.L. Yi, G.S. Hao, Y.Y. Sun, J.Q. Wang, E.-H. Han, W. Ke, The role of reversed austenite in hydrogen embrittlement fracture of S41500 martensitic stainless steel. *Acta Mater.* **139**, 188–195 (2017)
35. M.O.H.S.E.N Dadfarnia, A.K.I.H.I.D.E. Nagao, B.P. Somerday, P.E. Schembri, J.W. Foulk III, K.A. Nibur, D.K. Balch, R.O. Ritchie, P. Sofronis, Modeling hydrogen-induced fracture and

- crack propagation in high strength steels, in *Materials Performance in Hydrogen Environments, Proceedings of the 2016 International Hydrogen Conference, Jackson Lake Lodge, Moran, WY, USA* (ASM International, Warrendale, PA 2017), pp. 572–80
36. J. Rehr, K. Mraczek, A. Pichler, E. Werner, Mechanical properties and fracture behavior of hydrogen charged AHSS/UHSS grades at high-and low strain rate tests. *Mater. Sci. Eng. A* **590**, 360–367 (2014)
  37. D. Sasaki, M. Koyama, H. Noguchi, Factors affecting hydrogen-assisted cracking in a commercial tempered martensitic steel: Mn segregation, MnS, and the stress state around abnormal cracks. *Mater. Sci. Eng. A* **640**, 72–81 (2015)
  38. X. Li, J. Zhang, E. Akiyama, Y. Wang, Q. Li, Microstructural and crystallographic study of hydrogen-assisted cracking in high strength PSB1080 steel. *Int. J. Hydrogen Energy* **43**(37), 17898–17911 (2018)
  39. L.B. Peral, A. Zafra, J. Belzunce, C. Rodríguez, Effects of hydrogen on the fracture toughness of CrMo and CrMoV steels quenched and tempered at different temperatures. *Int. J. Hydrogen Energy* **44**(7), 3953–3965 (2019)
  40. J. Song, W.A. Curtin, Atomic mechanism and prediction of hydrogen embrittlement in iron. *Nat. Mater.* **12**(2), 145–151 (2013)
  41. R. Falkenberg, W. Brocks, W. Dietzel, I. Scheider, Modelling the effect of hydrogen on ductile tearing resistance of steels: dedicated to Professor Dr. Hermann Riedel on the occasion of his 65th birthday. *Int. J. Mater. Res.* **101**(8), 989–996 (2010)
  42. L. Jemblie, V. Olden, O.M. Akselsen, A review of cohesive zone modelling as an approach for numerically assessing hydrogen embrittlement of steel structures. *Philos. Trans. R. Soc. A Math. Phys. Eng. Sci.* **375**(2098), 20160411 (2017)
  43. Y. Hu, C. Dong, H. Luo, K. Xiao, P. Zhong, X. Li, Study on the hydrogen embrittlement of Aermet100 using hydrogen permeation and SSRT techniques. *Metall. Mater. Trans. A* **48**(9), 4046–4057 (2017)
  44. P. Novak, R. Yuan, B.P. Somerday, P. Sofronis, R.O. Ritchie, A statistical, physical-based, micro-mechanical model of hydrogen-induced intergranular fracture in steel. *J. Mech. Phys. Solids* **58**(2), 206–226 (2010)
  45. H. Yu, J.S. Olsen, A. Alvaro, L. Qiao, J. He, Z. Zhang, Hydrogen informed Gurson model for hydrogen embrittlement simulation. *Eng. Fract. Mech.* **217**, 106542 (2019)
  46. H. Khoramshad, J. Akbardoost, M.R. Ayatollahi, Size effects on parameters of cohesive zone model in mode I fracture of limestone. *Int. J. Damage Mech* **23**(4), 588–605 (2014)
  47. H.K. Birnbaum, P. Sofronis, Hydrogen-enhanced localized plasticity—a mechanism for hydrogen-related fracture. *Mater. Sci. Eng. A* **176**(1–2), 191–202 (1994)
  48. H. Yu, J.S. Olsen, J. He, Z. Zhang, Hydrogen-microvoid interactions at continuum scale. *Int. J. Hydrogen Energy* **43**(21), 10104–10128 (2018)
  49. A.L. Gurson, Continuum theory of ductile rupture by void nucleation and growth: part I—yield criteria and flow rules for porous ductile media. *J. Eng. Mater. Technol.* **99**(1), 2–15 (1977)
  50. V. Tvergaard, A. Needleman, Analysis of the cup-cone fracture in a round tensile bar. *Acta Metall.* **32**(1), 157–169 (1984)
  51. J. Venezuela, C. Tapia-Bastidas, Q. Zhou, T. Depover, K. Verbeken, E. Gray, A. Atrens, Determination of the equivalent hydrogen fugacity during electrochemical charging of 3.5 NiCrMoV steel. *Corros. Sci.* **132**, 90–106 (2018)
  52. A. Atrens, Q. Liu, C. Tapia-Bastidas, E. Gray, B. Irwanto, J. Venezuela, Q. Liu, Influence of hydrogen on steel components for clean energy. *Corros. Mater. Degrad.* **1**(1), 3–26 (2018)
  53. G. Hachet, A. Metsue, A. Oudriss, X. Feaugas, Influence of hydrogen on the elastic properties of nickel single crystal: A numerical and experimental investigation. *Acta Mater.* **148**, 280–288 (2018)
  54. T. Depover, K. Verbeken, Hydrogen trapping and hydrogen induced mechanical degradation in lab cast Fe–C–Cr alloys. *Mater. Sci. Eng. A* **669**, 134–149 (2016)
  55. T. Depover, E. Wallaert, K. Verbeken, Fractographic analysis of the role of hydrogen diffusion on the hydrogen embrittlement susceptibility of DP steel. *Mater. Sci. Eng. A* **649**, 201–208 (2016)
  56. K. Ichii, M. Koyama, C.C. Tasan, K. Tsuzaki, Comparative study of hydrogen embrittlement in stable and metastable high-entropy alloys. *Scr. Mater.* **150**, 74–77 (2018)
  57. J. Yamabe, M. Yoshikawa, H. Matsunaga, S. Matsuoka, Hydrogen trapping and fatigue crack growth property of low-carbon steel in hydrogen-gas environment. *Int. J. Fatigue* **102**, 202–213 (2017)
  58. M. Koyama, E. Akiyama, Y.K. Lee, D. Raabe, K. Tsuzaki, Overview of hydrogen embrittlement in high-Mn steels. *Int. J. Hydrogen Energy* **42**(17), 12706–12723 (2017)
  59. M. Dadfarnia, A. Nagao, S. Wang, M.L. Martin, B.P. Somerday, P. Sofronis, Recent advances on hydrogen embrittlement of structural materials. *Int. J. Fract.* **196**(1–2), 223–243 (2015)
  60. G. Bilotta, G. Henaff, D. Halm, M. Arzaghi, Experimental measurement of out-of-plane displacement in crack propagation under gaseous hydrogen. *Int. J. Hydrogen Energy* **42**(15), 10568–10578 (2017)
  61. J.A. Ronevich, B.P. Somerday, C.W. San Marchi, Effects of microstructure banding on hydrogen assisted fatigue crack growth in X65 pipeline steels. *Int. J. Fatigue* **82**, 497–504 (2016)
  62. B.P. Somerday, P. Sofronis, K.A. Nibur, C. San Marchi, R. Kirchheim, Elucidating the variables affecting accelerated fatigue crack growth of steels in hydrogen gas with low oxygen concentrations. *Acta Mater.* **61**(16), 6153–6170 (2013)
  63. Y. Ogawa, D. Birenis, H. Matsunaga, A. Thøgersen, Ø. Prytz, O. Takakuwa, J. Yamabe, Multi-scale observation of hydrogen-induced, localized plastic deformation in fatigue-crack propagation in a pure iron. *Scr. Mater.* **140**, 13–17 (2017)
  64. D. Wan, Y. Deng, A. Barnoush, Hydrogen embrittlement effect observed by IHPCon a ferritic alloy. *Scr. Mater.* **151**, 24–27 (2018)
  65. T. Depover, D. Hajilou, D. Wan, A. Wang, K.V. Barnoush, Assessment of the potential of hydrogen plasma charging as compared to conventional electrochemical hydrogen charging on dual phase steel. *Mater. Sci. Eng. A* **754**, 613–621 (2019)
  66. M. Asadipoor, A.P. Anaraki, J. Kadkhodapour, S.M.H. Sharifi, A. Barnoush, Macro-and microscale investigations of hydrogen embrittlement in X70 pipeline steel by in-situ and ex-situ hydrogen charging tensile tests and in-situ electrochemical micro-cantilever bending test. *Mater. Sci. Eng. A* **772**, 138762 (2020)
  67. R. Silverstein, D. Eliezer, E. Tal-Gutelmacher, Hydrogen trapping in alloys studied by thermal desorption spectrometry. *J. Alloys Compd.* **747**, 511–522 (2018)
  68. A. Laureys, E. Van den Eeckhout, R. Petrov, K. Verbeken, Effect of deformation and charging conditions on crack and blister formation during electrochemical hydrogen charging. *Acta Mater.* **127**, 192–202 (2017)
  69. T. Depover, K. Verbeken, The detrimental effect of hydrogen at dislocations on the hydrogen embrittlement susceptibility of Fe–CX alloys: An experimental proof of the HELP mechanism. *Int. J. Hydrogen Energy* **43**(5), 3050–3061 (2018)
  70. A. Needleman, V. Tvergaard, An analysis of ductile rupture modes at a crack tip. *J. Mech. Phys. Solids* **35**(2), 151–183 (1987)
  71. V. Tvergaard, On localization in ductile materials containing spherical voids. *Int. J. Fract.* **18**(4), 237–252 (1982)
  72. J. Faleskog, X. Gao, C.F. Shih, Cell model for nonlinear fracture analysis—I. Micromechanics calibration. *Int. J. Fract.* **89**(4), 355–373 (1998)
  73. M.R. Ayatollahi, A.C. Darabi, H.R. Chamani, J. Kadkhodapour, 3D micromechanical modeling of failure and damage evolution

- in dual phase steel based on a real 2D microstructure. *Acta Mech. Solida Sin.* **29**(1), 95–110 (2016)
74. N. Vajragupta, V. Uthaisangsuk, B. Schmaling, S. Münstermann, A. Hartmaier, W. Bleck, A micromechanical damage simulation of dual phase steels using XFEM. *Comput. Mater. Sci.* **54**, 271–279 (2012)
  75. V. Uthaisangsuk, U. Pahl, W. Bleck, Micromechanical modelling of damage behaviour of multiphase steels. *Comput. Mater. Sci.* **43**(1), 27–35 (2008)
  76. C. Soyarslan, M.M. Gharbi, A.E. Tekkaya, A combined experimental–numerical investigation of ductile fracture in bending of a class of ferritic–martensitic steel. *Int. J. Solids Struct.* **49**(13), 1608–1626 (2012)
  77. I. Tsouppis, M. Merklein, A new way for the adaption of inverse identified GTN-parameters to bending processes, in *13th International LS-DYNA Users Conference* (2014), (pp. 1–14)
  78. S. Katani, S. Ziaei-Rad, N. Nouri, N. Saeidi, J. Kadkhodapour, N. Torabian, S. Schmauder, Microstructure modelling of dual-phase steel using SEM micrographs and Voronoi polycrystal models. *Metallogr. Microstruct. Anal.* **2**(3), 156–169 (2013)
  79. G. Avramovic-Cingara, C.A. Saleh, M.K. Jain, D.S. Wilkinson, Void nucleation and growth in dual-phase steel 600 during uniaxial tensile testing. *Metall. Mater. Trans. A* **40**(13), 3117 (2009)
  80. L.S. Morrissey, S.M. Handrigan, S. Nakhla, Quantifying void formation and changes to microstructure during hydrogen charging: a precursor to embrittlement and blistering. *Metall. Mater. Trans. A* **50**(3), 1460–1467 (2019)
  81. E. Maire, S. Grabon, J. Adrien, P. Lorenzino, Y. Asanuma, O. Takakuwa, H. Matsunaga, Role of hydrogen-charging on nucleation and growth of ductile damage in austenitic stainless steels. *Materials* **12**(9), 1426 (2019)
  82. T. Kumamoto, M. Koyama, K. Tsuzaki, Strain rate sensitivity of microstructural damage evolution in a dual-phase steel pre-charged with hydrogen. *Procedia Struct. Integr.* **13**, 710–715 (2018)
  83. F. Rahimidehgolan, G. Majzoobi, F. Alinejad, J. Fathi Sola, Determination of the constants of GTN damage model using experiment, polynomial regression and kriging methods. *Appl. Sci.* **7**(11), 1179 (2017)
  84. M. Abbasi, M. Ketabchi, H. Izadkhah, D.H. Fatmehsaria, A.N. Aghbash, Identification of GTN model parameters by application of response surface methodology. *Procedia Eng.* **10**, 415–420 (2011)
  85. <https://www.ssab.com/products/brands/docol/products/docol-1200M>. Accessed 15 July 2019
  86. C.J. McMahon Jr., Hydrogen-induced intergranular fracture of steels. *Eng. Fract. Mech.* **68**(6), 773–788 (2001)
  87. D.E. Jiang, E.A. Carter, First principles assessment of ideal fracture energies of materials with mobile impurities: implications for hydrogen embrittlement of metals. *Acta Mater.* **52**(16), 4801–4807 (2004)
  88. O. Takakuwa, J. Yamabe, H. Matsunaga, Y. Furuya, S. Matsuoka, Comprehensive understanding of ductility loss mechanisms in various steels with external and internal hydrogen. *Metall. Mater. Trans. A* **48**(11), 5717–5732 (2017)

**Publisher's Note** Springer Nature remains neutral with regard to jurisdictional claims in published maps and institutional affiliations.